

Faraday rotation at low frequencies: magnetoionic material of the large FR II radio galaxy PKS J0636–2036

S. P. O’Sullivan,^{1,2★} E. Lenc,^{3,4} C. S. Anderson,⁵ B. M. Gaensler,^{4,6} and T. Murphy^{3,4}

¹Hamburger Sternwarte, Universität Hamburg, Gojenbergsweg 112, Hamburg 21029, Germany

²Instituto de Astronomía, Universidad Nacional Autónoma de México (UNAM), A.P. 70-264, 04510 México, D.F., México

³Sydney Institute for Astronomy, School of Physics, The University of Sydney, NSW 2006, Australia

⁴ARC Centre of Excellence for All-sky Astrophysics (CAASTRO)

⁵CSIRO Astronomy & Space Science, Kensington, Perth 6151, Australia

⁶Dunlap Institute for Astronomy and Astrophysics, University of Toronto, 50 St. George Street, Toronto, ON M5S 3H4, Canada

Accepted XXX. Received YYY; in original form ZZZ

ABSTRACT

We present a low-frequency, broadband polarization study of the FR II radio galaxy PKS J0636–2036 ($z = 0.0551$), using the Murchison Widefield Array (MWA) from 70 to 230 MHz. The northern and southern hotspots (separated by $\sim 14.5'$ on the sky) are resolved by the MWA ($3'.3$ resolution) and both are detected in linear polarization across the full frequency range. A combination of Faraday rotation measure (RM) synthesis and broadband polarization model-fitting are used to constrain the Faraday depolarization properties of the source. For the integrated southern hotspot emission, two RM component models are strongly favoured over a single RM component, and the best-fitting model requires Faraday dispersions of approximately 0.7 and 1.2 rad m^{-2} (with a mean RM of $\sim 50 \text{ rad m}^{-2}$). High resolution imaging at $5''$ with the ATCA shows significant sub-structure in the southern hotspot and highlights some of the limitations in the polarization modelling of the MWA data. Based on the observed depolarization, combined with extrapolations of gas density scaling-relations for group environments, we estimate magnetic field strengths in the intergalactic medium between ~ 0.04 and $0.5 \mu\text{G}$. We also comment on future prospects of detecting more polarized sources at low frequencies.

Key words: radio continuum: galaxies – galaxies: magnetic fields – galaxies: active – galaxies: jets – techniques: polarimetric – galaxies: individual (PKS J0636–2036)

1 INTRODUCTION

Active galactic nuclei (AGN) can eject jets of relativistic plasma powered by the central supermassive black hole of the host galaxy. These AGN jets have sufficient energy to significantly impact the evolution of the host galaxy and its immediate environment by heating the interstellar and intergalactic gas that might otherwise cool and eventually form stars (e.g. Kronberg et al. 2001; Croton et al. 2006). Determining the exact mechanism(s) by which these AGN jets can transfer their energy to the environment is important for understanding the role of AGN in the evolution of galaxies (Fabian 2012; McNamara & Nulsen 2012; Heckman & Best 2014). Shocks, sound waves, cosmic rays, as well as entrainment and large scale mixing of gas by the jets (and lobes) have been studied as potential mechanisms for depositing the latent AGN jet energy into its en-

vironment (e.g. Brüggén & Kaiser 2002; Fabian et al. 2003; Enßlin et al. 2011; Ruszkowski et al. 2017).

The structure of AGN jets and lobes is illuminated by particle acceleration processes that generate synchrotron emission that is easily detected at radio wavelengths. This synchrotron emission is intrinsically highly linearly polarized, which enables radio spectropolarimetry observations to provide a sensitive probe of thermal plasma via the effect of Faraday rotation. The Faraday rotation is detected through the change in the linear polarization angle ($\Delta\psi$) as a function of wavelength-squared (λ^2), where $\Delta\psi = \text{RM}\lambda^2$, with the Faraday rotation measure (RM) defined as

$$\text{RM}_{[\text{rad m}^{-2}]} = 0.812 \int_{\text{source}}^{\text{telescope}} n_e [\text{cm}^{-3}] B_{\parallel} [\mu\text{G}] dl [\text{pc}] \quad (1)$$

where B_{\parallel} is the line-of-sight magnetic field, n_e is the free electron number density, and l is the path length through the magnetoionic medium.

Since the precision with which the Faraday rotation measure can be determined depends on the total wavelength-

★ E-mail: shane@hs.uni-hamburg.de

squared coverage, low-frequency radio telescopes (with frequencies less than 300 MHz) can outperform traditional centimetre radio facilities by more than two orders of magnitude in this regard (Brentjens & de Bruyn 2005). Finding extragalactic polarized sources at low radio frequencies has been challenging to date due to the often poor angular resolution, the influence of the ionosphere, and the expected strong effect of Faraday depolarization (c.f. Farnsworth et al. 2011; de Bruyn 2012; Gießbübel et al. 2013). However, recent advancements in low frequency radio interferometers, for example the Murchison Widefield Array (MWA; Tingay et al. 2013) and the Low Frequency Array (LOFAR; van Haarlem et al. 2013) show that it is possible to detect extragalactic polarized sources at these frequencies (e.g. Bernardi et al. 2013; Mulcahy et al. 2014; Jelić et al. 2015; Orrù et al. 2015; Lenc et al. 2016).

In this paper, we study the brightest polarized source detected to date at low frequencies, PKS J0636–2036, using the MWA telescope from 70 to 230 MHz. This is the first broadband polarization and Faraday rotation analysis of a radio galaxy at such low radio frequencies, providing key constraints on the thermal gas properties of radio galaxies, and important insights for studies in this area with current and future radio telescopes (e.g. SKA1-low¹).

PKS J0636–2036 is a nearby FR II radio galaxy identified with an isolated elliptical host galaxy at $z = 0.0551$ (Schilizzi & McAdam 1975; Kronberg et al. 1986). The radio galaxy has two bright, roughly co-linear hotspots at either ends of the radio structure connected by fainter bridges of radio emission (the lobes), while the host galaxy has broad optical emission lines and extended emission-line gas within $20''$ of the nucleus (Baum et al. 1988). The radio luminosity at 1.4 GHz is $L_{1.4\text{GHz}} \sim 6 \times 10^{25} \text{ W Hz}^{-1}$. The southern hotspot is the brightest feature of the source, and the southern lobe is $\sim 100''$ longer on the sky than the northern lobe. The total size of the radio galaxy is $\sim 870''$, which led it to be listed as a Giant Radio Galaxy (GRG) in early studies (Danziger et al. 1978), although with the cosmology used in this paper the projected linear size is $\sim 957 \text{ kpc}$. GRGs are typically defined as radio sources with linear sizes of $\gtrsim 1 \text{ Mpc}$, likely due to their jets propagating in a low density environment (e.g. Mack et al. 1998; Schoenmakers et al. 2000; Subrahmanyam et al. 2008; Machalski et al. 2011).

In Section 2, we describe the MWA observations and data reduction, as well as a description of high angular resolution observations with the Australia Telescope Compact Array (ATCA). Section 3 describes our general approach to the broadband polarization modelling. Section 4 presents the results for the northern and southern hotspot of PKS J0636–2036. In Section 5 we present various scenarios to explain the broadband polarization data, and discuss the likelihoods and implications of these scenarios in Section 6. The conclusions are listed in Section 7. Throughout this paper, we assume a flat Λ CDM cosmology with $H_0 = 67.3 \text{ km s}^{-1} \text{ Mpc}^{-1}$, $\Omega_M = 0.315$ and $\Omega_\Lambda = 0.685$ (Planck Collaboration et al. 2014). At the redshift of the source, $1''$ corresponds to a linear size of 1.1 kpc. We define the total intensity spectral index, α , such that the ob-

served total intensity (I) at frequency ν follows the relation $I_\nu \propto \nu^{+\alpha}$.

2 OBSERVATIONS AND DATA REDUCTION

2.1 MWA Observations

The Murchison Widefield Array (MWA) is located at the Murchison Radio Observatory in Western Australia. At the time of observation, the MWA consisted of 128 tiles (with a maximum baseline length of $\sim 3 \text{ km}$), where each tile has a regular 4×4 grid of dual-polarization dipoles (Tingay et al. 2013).

We used archival² GLEAM (A Galactic and Extragalactic All-Sky MWA) survey visibility data ranging from 72 MHz to 231 MHz (Wayth et al. 2015; Hurley-Walker et al. 2017). Our primary target, PKS J0636–2036, drifted within the half-power beam-width on 2013 November 25 between 17:37 and 19:13 UTC. The observing specifications are listed in Table 1.

The data was flagged using AOFLAGGER (Offringa et al. 2012) to remove radio frequency interference (RFI) and channels affected by the poly-phase filter bank (Ord et al. 2015). In all, approximately 25% of data was flagged although only a small fraction of this was due to actual RFI (Offringa et al. 2015).

We used the real-time calibration and imaging system (RTS; Mitchell et al. 2008; Ord et al. 2010) for bandpass and gain calibration on a per 2-minute snapshot basis. We used a local sky model centered on the inner 20° of the primary beam and taking an ensemble of the 30 most significant sources taken from the MWA Commissioning Survey (Hurley-Walker et al. 2014). Visibility data from baselines shorter than 50λ were down-weighted to improve calibration in the presence of diffuse structure. We estimate the uncertainty on the absolute calibration to be better than 10%.

Imaging was also carried out with the RTS with a taper to down-weight baselines above 700λ and a lower baseline length limit of 50λ . The baseline restrictions provide a near-constant beam size across all frequency bands (Table 2) and limit contamination from large scale structure. To avoid bandwidth depolarization, all bands were imaged at the full 40 kHz spectral resolution.

To correct for ionospheric Faraday rotation we estimated the ionospheric contribution to the RM with RMEXTRACT³. The ionospheric component of the RM was then de-rotated from the Stokes Q and U image cubes in each 2 minute snapshot. Once corrected, the image cubes were integrated in time. Predictions of ionospheric Faraday rotation are typically accurate to within $\sim 0.2 \text{ rad m}^{-2}$ (Lenc et al. 2016). For the night-time, near-zenith observations presented here, Lenc et al. (2017) showed that the predictive accuracy of the variable component of ionospheric RM was $\sim 0.03 \text{ rad m}^{-2}$. Similarly, they demonstrated that if the accuracy were worse than $\sim 0.085 \text{ rad m}^{-2}$ then the southern hotspot would completely depolarize in the 89 MHz MWA

¹ <http://skatelescope.org/>

² <http://mwa-metadata01.pawsey.org.au/admin/observation/observations>

³ <https://github.com/maaijke/RMextract>

Table 1. Summary of observing specifications for each observing band. The lowest and highest observing frequency are specified by ν_{\min} and ν_{\max} , respectively. BW_{chan} specifies the channel bandwidth used for imaging and t_{int} the overall on-source integration time (note that the ATCA data is spread over two pointings in order to image both the northern and southern hotspot). $\delta\phi$ and $|\phi_{\text{max}}|$ are the resolution and Faraday depth range available in each band when using the RM synthesis technique.

Array	Band (MHz)	ν_{\min} (MHz)	ν_{\max} (MHz)	BW_{chan} (MHz)	t_{int} (min)	$\delta\phi$ (rad m ⁻²)	$ \phi_{\text{max}} $ (rad m ⁻²)
MWA	89	74.615	102.935	0.04	12	0.45	100
MWA	118	103.135	133.655	0.04	14	1.0	264
MWA	154	138.995	169.475	0.04	16	2.3	647
MWA	185	169.715	200.195	0.04	16	3.9	1178
MWA	216	200.435	230.915	0.04	8	6.3	1940
ATCA	2150	1284	3012	32.0	230	78	661

Table 2. Summary of imaging parameters for each observing band. r is the robustness weighting used for imaging. σ is the image rms noise for each of the Stokes parameters when utilizing the entire available bandwidth. θ_{maj} and θ_{min} are the major and minor axis of the synthesized beam (FWHM), respectively. PA is the position angle of the synthesized beam measured from north to east.

Array	Band (MHz)	r	σ_i (mJy beam ⁻¹)	σ_q (mJy beam ⁻¹)	σ_u (mJy beam ⁻¹)	σ_v (mJy beam ⁻¹)	θ_{maj}	θ_{min}	PA (deg)
MWA	89	-1	340	35	36	34	4.3'	4.0'	-70
MWA	118	-1	192	12	12	12	3.7'	3.5'	-47
MWA	154	-1	159	7.6	7.8	6.5	3.5'	3.3'	-74
MWA	185	-1	152	6.0	6.1	5.2	3.4'	3.3'	-87
MWA	216	-1	151	7.1	6.0	5.4	3.4'	3.3'	-80
ATCA	2150	0	3.8	0.5	0.9	0.2	5.0''	5.0''	0
ATCA	2150	0	9.2	0.8	1.0	0.3	25.0''	25.0''	0

band. These tests do not preclude the possibility of a constant offset error in the ionosphere RM prediction, however, as all MWA bands were observed over the same period they would all exhibit the same offset.

2.2 ATCA Observations

PKS J0636-2036 was observed using Directors Time (project CX317) on 2015 February 27 from 04:40-14:47 UTC using the Australia Telescope Compact Array (ATCA) in a 6 km configuration (configuration 6C). The Compact Array Broadband Backend (CABB; Wilson et al. 2011) was used with 2048 MHz bandwidth (1 MHz channels) centered at 2.1 GHz (16 cm). In total, 12 × 10 minute scans were taken of the southern hotspot and 11 × 10 minutes scans of northern hotspot.

A 15 minute scan of the standard flux density calibration source PKS B1934-638 was used for calibration. Primary flux density calibration and data flagging for radio frequency interference was performed using standard calibration procedures for the ATCA in the data reduction package Miriad (Sault et al. 1995). The observations suffered from significant RFI at the lower end of the band and the first ~150 channels were flagged.

Time-dependent calibration was performed by first generating spectral models for both the northern and southern hotspots with the task MFCLEAN and then using this model to perform phase-only self-calibration. Once calibrated, the visibilities were averaged down to 64 × 32 MHz channels and full-Stokes image cubes were generated and deconvolved using the task CLEAN. The resulting image cubes were restored

with a 5'' beam to enable the high resolution structure of the polarized hot spot to be studied. They were also restored with a 25'' beam to study the unresolved properties of the hotspot.

To determine the effect of ionospheric Faraday rotation we used RMEXTRACT to estimate the RM component of the ionosphere over the course of the ATCA observing period. The mean shift in RM as a result of ionospheric Faraday rotation was estimated to be -2.5 rad m⁻² and all RM measurements made with the ATCA were adjusted to account for this.

3 POLARIZATION MODEL-FITTING APPROACH

In order to model the broadband polarization data, we consider several different polarization models that describe different types of Faraday depolarization. In particular, we follow the algorithm described in O’Sullivan et al. (2017), where they use a general model that can describe Faraday effects internal or external to the emission region, from both uniform and turbulent magnetic fields. The complex polarization equation for this model is

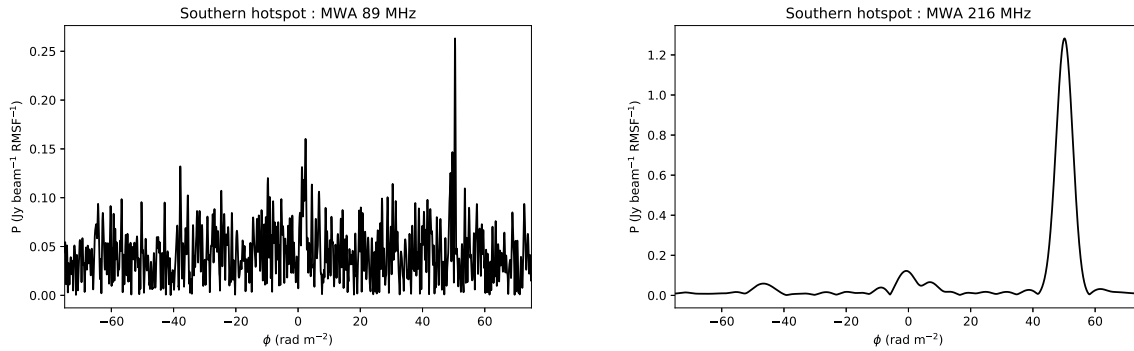
$$P = p_0 e^{2i(\psi_0 + \text{RM}\lambda^2)} \frac{\sin \Delta\text{RM}\lambda^2}{\Delta\text{RM}\lambda^2} e^{-2\sigma_{\text{RM,B}}^2 \lambda^4} \quad (2)$$

where for each complex polarization component (P) or ‘RM component’, p_0 is the intrinsic degree of polarization and ψ_0 is the intrinsic polarization angle. The parameter ΔRM usually describes internal Faraday depolarization in the presence of a uniform magnetic field, but can also be consistent

Table 3. Summary of polarization properties of the southern (subscript s) and northern (subscript n) hotspots in each of the observed bands. S is the total intensity, P is the polarized intensity, p is the polarized fraction and RM is the measured Faraday rotation.

Array	Band (MHz)	S_s (Jy)	P_s (mJy)	p_s	RM_s (rad m ⁻²)	S_n (Jy)	P_n (mJy)	p_n	RM_n (rad m ⁻²)
MWA	89	29.6	262	0.9%	+49.4 ± 1.2	14.9	169	1.1%	+35.9 ± 0.03
MWA	118	22.6	451	2.0%	+50.0 ± 0.02	10.2	146	1.4%	+36.0 ± 0.03
MWA	154	17.8	558	3.1%	+50.1 ± 0.04	7.8	215	2.7%	+36.3 ± 0.03
MWA	185	15.7	985	6.3%	+50.1 ± 0.03	6.8	192	2.9%	+36.5 ± 0.1
MWA	216	13.9	1283	9.2%	+50.2 ± 0.05	6.0	142	2.4%	+36.1 ± 0.3
NVSS	1400	3.01	456	15.1%	+47.1 ± 1.9	1.53	164	10.7%	+34.8 ± 7.2

Note: NVSS RM values not corrected for the ionospheric RM contribution.

**Figure 1.** Faraday dispersion functions for the southern hotspot of PKS J0636–2036, shown for the lowest (left) and highest (right) frequency GLEAM bands.

with external Faraday depolarization caused by a linear gradient in RM across the emission region (e.g. Sokoloff et al. 1998; Schnitzeler et al. 2015). The parameter $\sigma_{RM,B}$ is used to describe Faraday depolarization from RM variations due to a turbulent magnetic field, a process often referred to as external Faraday dispersion or ‘Burn-law’ depolarization (Burn 1966; Laing et al. 2008).

As described in Tribble (1991) and Sokoloff et al. (1998), the assumptions underlying the ‘Burn-law’ are expected to break down in the long wavelength regime ($2\sigma_{RM}\lambda^2 \gg 1$, $p(\lambda^2)/p(0) \ll 0.5$). Therefore, we also consider polarization models that include the expected transition from an exponential decline to a power-law decline in $p(\lambda^2)$, as described in eqn. 3 of Tribble (1992). In this case,

$$P = \mathcal{P} \frac{\sin \Delta RM \lambda^2}{\Delta RM \lambda^2} \left(\frac{1 - e^{-S - 4\sigma_{RM,T}^2 \lambda^4}}{1 + 4\sigma_{RM,T}^2 \lambda^4 / S} + e^{-S - 4\sigma_{RM,T}^2 \lambda^4} \right)^{1/2} \quad (3)$$

where $\mathcal{P} = p_0 e^{2i(\psi_0 + RM\lambda^2)}$ and $\sigma_{RM,T}$ is used to describe Faraday depolarization following the ‘Tribble-law’, with the parameter $S = s_0/t$ depending on the resolution of the observations (t) and the scale size of the RM fluctuations (s_0). For example, as $S \rightarrow 0$ the RM structure becomes fully unresolved and the ‘Burn-law’ behaviour is recovered, while as $S \rightarrow \infty$ the RM structure becomes fully resolved and there is no depolarization.

In the ‘short-wavelength’ regime ($p(\lambda^2)/p_0 > 0.5$), the σ_{RM} and ΔRM parameters produce equivalent amounts of depolarization for $\Delta RM \sim 3.22\sigma_{RM}$. Furthermore, the ΔRM parameter can describe a linear gradient in RM across a flat

beam profile, but to describe the more realistic case of a Gaussian beam profile ΔRM needs to be divided by a factor of 1.35 (Sokoloff et al. 1998). In the case of internal Faraday rotation, this correction factor is not required.

In this work, we consider up to a maximum of two RM component models, using Eqns. 2 & 3 and combinations thereof (e.g. $P = P_1 + P_2$). To evaluate the quality of fit and to discriminate between models with different numbers of parameters, we use the reduced- χ -squared values (χ_r^2) and the Bayesian Information Criterion (BIC), as described in O’Sullivan et al. (2012). The model with the lowest BIC and χ_r^2 values was selected as the best fitting model (e.g. Raftery 1995).

4 RESULTS

Rotation Measure (RM) Synthesis (Brentjens & de Bruyn 2005) was used to determine the Faraday dispersion function (FDF), which is the polarized intensity as a function of Faraday depth (Burn 1966), for each pixel in each image cube. To decrease the effect of sidelobes in Faraday space, the RM cubes were deconvolved using RM CLEAN (Heald 2009). With the combined ionospheric calibration and RM synthesis technique, polarization was detected in both the northern and southern hot spot of PKS J0636–2036 across each of the five MWA observing bands and in the ATCA data (faint polarized emission was also detected in the northern lobe/bridge in the two highest MWA bands, and is summarised in Section 4.2).

The peak polarized intensity and RM was measured at

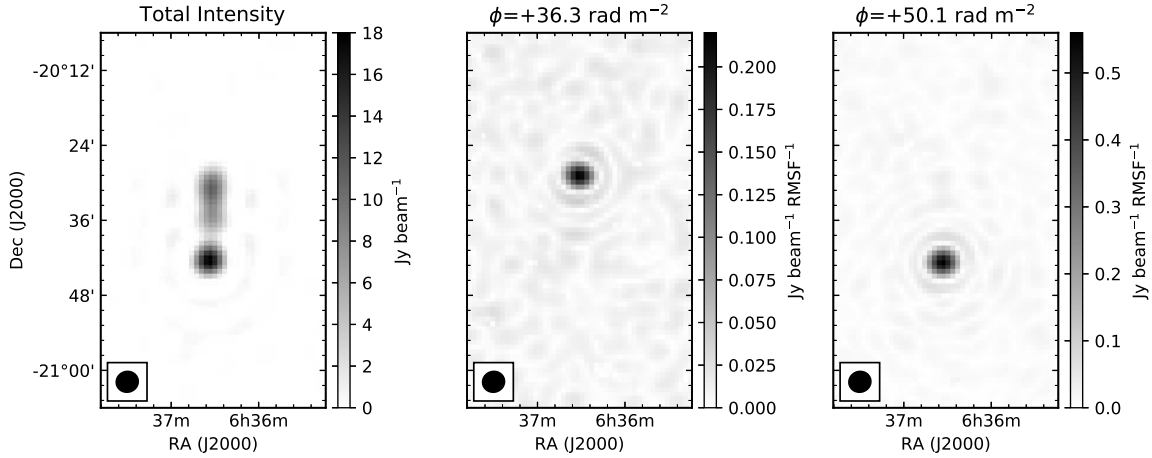


Figure 2. Total intensity map of PKS J0636–2036 and the associated polarized intensity maps of the source taken at Faraday depths of $\phi = +36.3 \text{ rad m}^{-2}$ and $+50.1 \text{ rad m}^{-2}$ (corrected for ionospheric effects). All images were processed using robust visibility weighting (robustness = -1) in the 154 MHz band.

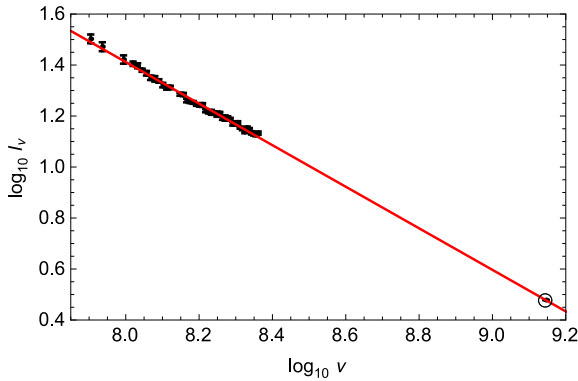


Figure 3. Stokes I flux versus frequency for the southern hotspot of PKS J0636–2036, from MWA and NVSS at $3'.3$ resolution. The NVSS data point is highlighted by a circle in the bottom left corner with an error of $0.5 \text{ mJy beam}^{-1}$. The best fitting spectral index value is $\alpha = -0.815 \pm 0.007$.

J2000 $06^{\text{h}}36^{\text{m}}33^{\text{s}}.15$, $-20^{\circ}42'40''$ for the southern hotspot and $06^{\text{h}}36^{\text{m}}31^{\text{s}}.75$, $-20^{\circ}29'00''$ for the northern hotspot in each of the RM cubes and is summarised in Table 3. The Faraday dispersion function for the southern hotspot of PKS J0636–2036, which is the brighter of the two hotspots, is shown in Figure 1 for the lowest and highest MWA frequency bands. Figure 2 shows the total intensity image of PKS J0636–2036 and the polarized intensity maps for the northern and southern hot spots in the 154 MHz band at $+36.3$ and $+50.1 \text{ rad m}^{-2}$, respectively.

4.1 Southern Hotspot

Figure 3 shows the total intensity as a function of frequency for the MWA data of the southern hotspot, and also includes the NRAO VLA Sky Survey (NVSS) data at 1.4 GHz (Condon et al. 1998). The NVSS I , Q and U images at 1.4

GHz⁴ were convolved to the same beamsize as the MWA data ($\sim 3'.3$). The NVSS total intensity and fractional polarization data were then extracted at the same location as the peak polarized intensity of the southern hotspot in the MWA data (Table 3). This also provided a crucial additional data point at $\lambda^2 \simeq 0.046 \text{ m}^2$ to help constrain the polarization model-fitting. The solid line in Figure 3 shows the linear regression fit to the MWA and NVSS total intensity data, with a best-fitting total intensity spectral index $\alpha = -0.815 \pm 0.007$. There is no evidence for a turnover/cutoff in the total intensity spectrum down to 75 MHz; although we cannot rule out higher resolution observations at low frequencies revealing more interesting spectral structure for the hotspot (e.g. Harwood et al. 2016, 2017).

The total RM of the southern hotspot of $\sim 50 \text{ rad m}^{-2}$ (Table 3) is dominated by the Galactic foreground (Kronberg et al. 1986; Taylor et al. 2009), with the RM contribution local to the source expected to be much smaller given how far the source extends outside its host galaxy, in addition to the low galaxy-density environment in which the source resides (Baum et al. 1988). Thus, one of the best ways to study the magnetoionic material local to the source is through the Faraday depolarization observed across the MWA bands.

Figure 4 shows the MWA broadband polarization data in each channel for the southern hotspot (with the NVSS data point included). The q , u data oscillate rapidly because of the large RM, however, from the envelope of the data it is clear that there is significant depolarization across the MWA band, which ranges in wavelength-squared from ~ 1.7 to 16 m^2 . For comparison, this is > 300 times the wavelength-squared coverage in typical cm-wavelength observations with the ATCA (e.g. O’Sullivan et al. 2012).

Due to the lack of an absolute polarization angle calibrator, there are unknown offsets in the polarization angles measured between the MWA bands. This precludes us from doing qu -fitting on the full dataset. We expect that this can

⁴ <http://www.cv.nrao.edu/nvss/postage.shtml>

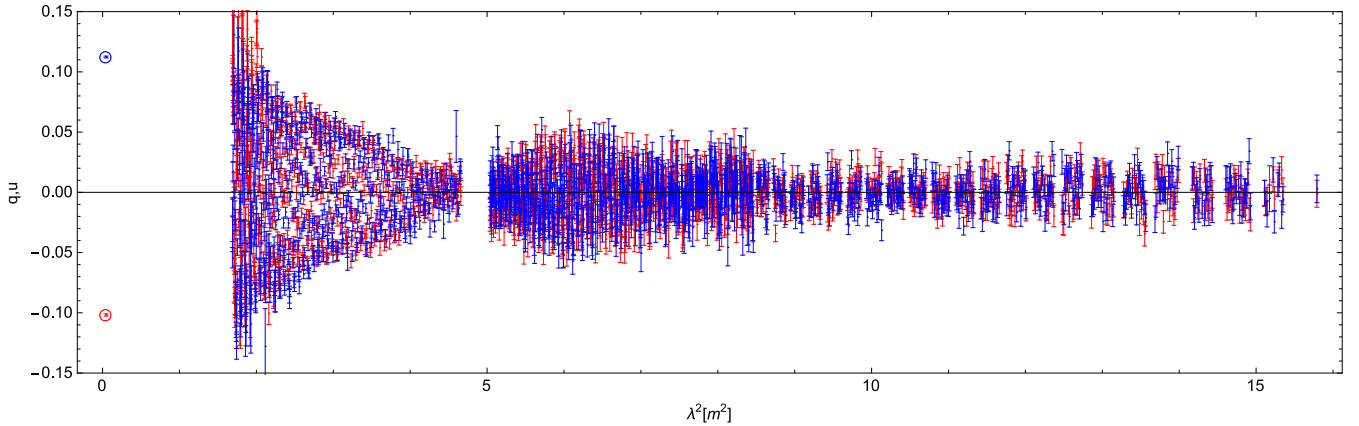


Figure 4. Variation in q (red) and u (blue) as a function of wavelength-squared (λ^2), for the southern hotspot. All data points are the raw 40 kHz MWA channel data from 75 to 230 MHz, except for the left-most points on the plot which are the NVSS q , u data at 1.4 GHz (highlighted by the red and blue circles).

be rectified in future when more brightly polarized sources are found and studied at low frequencies. Instead, we model the $p(\lambda^2)$ data (see Section 4.1.3) in conjunction with the RM synthesis results within each band (which are robust against the absolute polarization angle calibration).

To construct a reliable $p(\lambda^2)$ depolarization curve, we need to correct for both the instrumental polarization and the polarization bias. In order to isolate most of the instrumental polarization (which shows up mainly at $\text{RM} \sim 0 \text{ rad m}^{-2}$) from the real signal (at $\text{RM} \sim 50 \text{ rad m}^{-2}$), we used RM synthesis to coherently average the polarization data in small intervals across each MWA band (with 10 intervals across each band). We only retained those data points with signal to noise greater than 6 (Brentjens & de Bruyn 2005), and also corrected the degree of polarization for the effect of polarization bias, following George et al. (2012). By extracting the fractional polarization values at the peak in the RM synthesis spectrum near $\sim 50 \text{ rad m}^{-2}$, we were able to obtain a cleaner signal than if we just took the raw channel fractional polarization values. Figure 5 shows the resulting $p(\lambda^2)$ from the coherently averaged data from RM synthesis (blue points), overlaid on the raw channel data (uncorrected for bias and the effect of instrumental polarization).

4.1.1 ATCA imaging

The ATCA data at 16 cm enabled high angular resolution imaging of the southern hotspot at $5''$. This allowed us to resolve the total intensity and polarization structure, shown in Figure 6. The size of the hotspot region is $\sim 20 \text{ kpc}$, which is consistent with expectations based on self-similar models of FR II radio galaxies of this size (e.g. Hardcastle et al. 1998b; Kaiser & Alexander 1997). While the current ATCA data is excellent for resolving the structure of the hotspot, it is not sufficient for recovering all of the more diffuse lobe emission. Indeed the integrated total intensity emission is $\sim 15\%$ lower than expected from extrapolation of the best fitting line in Figure 3. Therefore, we only use the NVSS data as a more reliable ‘short-wavelength’ constraint in the polarization model fitting (Section 4.1.3)

RM synthesis was used on a pixel-by-pixel basis across

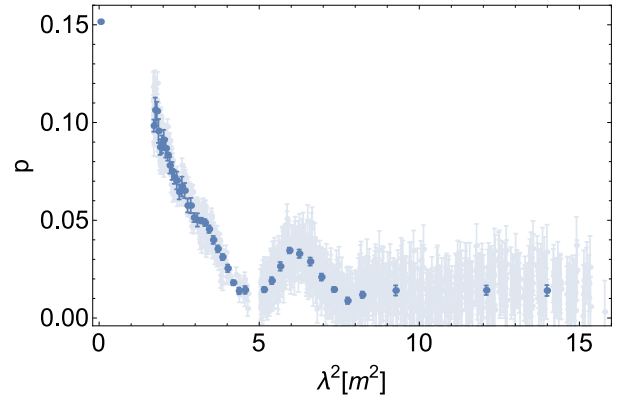


Figure 5. Plot of $p(\lambda^2)$ for the RM synthesis averaged data (blue points), after correcting for both the instrumental polarization and polarization bias. The translucent points show the raw MWA 40 kHz channel data. The NVSS data is included at $\lambda^2 \approx 0.046 \text{ m}^2$.

the hotspot emission to obtain the distributions of RM (corrected for ionospheric Faraday rotation; see Section 2.2) and fractional polarization, as well as the polarized intensity with the sensitivity of the full bandwidth. Figure 6 shows how the total intensity and polarization structure of the southern hotspot is split into two distinct regions (Region E & Region W), which is consistent with a previous VLA image at 5 GHz with $4''.5$ resolution (Kronberg et al. 1986). The peak polarized intensities of the two regions are slightly offset from the peak in total intensity, and the degree of polarization (Figure 7) increases sharply towards the outer edges of the regions, reaching maximum values of $\sim 45\%$. This type of structure is not uncommon for FR II hotspots (e.g. Rudnick et al. 1981; Rudnick 1988; Leahy et al. 1997), where at high angular resolution they are often resolved into ‘primary’ and ‘secondary’ hotspot regions (Laing 1989).

The RM distribution is shown in Figure 8, with the RM only shown where the polarized intensity is above $10\sigma_{QU}$ (where σ_{QU} is estimated from the rms noise level in the Faraday dispersion function of Q and U in regions far from the peak). The RM increases across Region E from the north-east to the south-west, while in Region W the

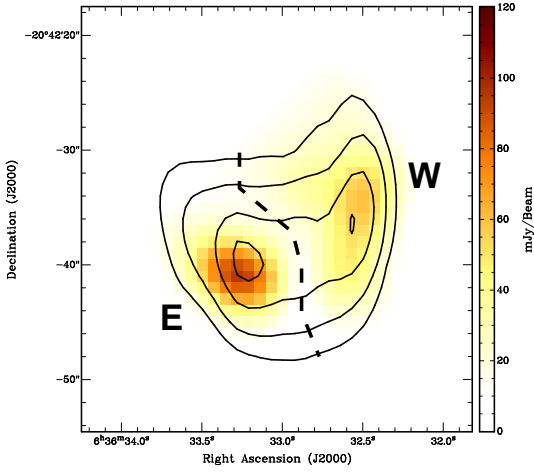


Figure 6. Total intensity (contours) and polarized intensity (colour-scale) of southern hotspot of PKS J0636–2036 at 5'' resolution with ATCA at 16 cm band. The dashed line denotes the separation between the eastern region (Region E) and the western region (Region W) of the hotspot.

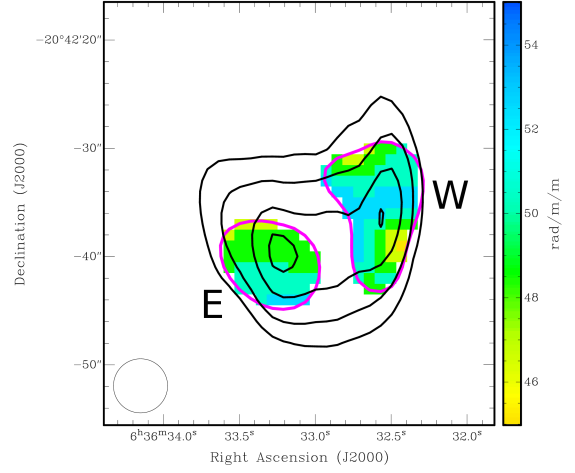


Figure 8. Total intensity (contours) and rotation measure distribution (colour-scale) of southern hotspot of PKS J0636–2036 at 5'' resolution with ATCA at 16 cm band. The magenta contours outline where the polarized intensity is greater than $10\sigma_{QU}$ for the two regions (E & W).

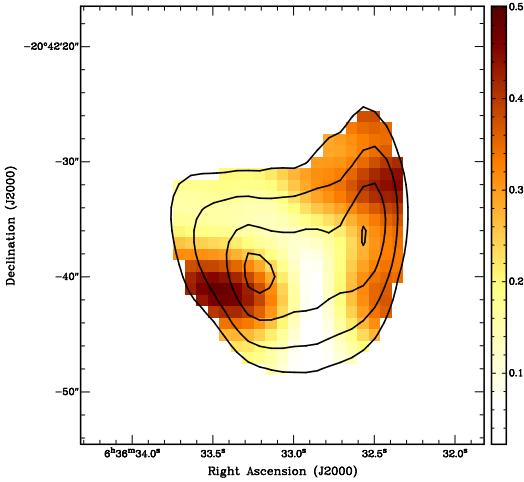


Figure 7. Total intensity (contours) and polarized fraction (colour-scale) of southern hotspot of PKS J0636–2036 at 5'' resolution with ATCA at 16 cm band.

RM peaks near the middle and decreases to the north-east and south-west. The intrinsic polarization angle distribution (Figure 9) was obtained by de-rotating the polarization angles to zero wavelength using the RM value of each pixel. This shows that the two brightly polarized regions have different intrinsic polarization angle distributions, and that the polarization angles are approximately orthogonal to the total intensity contours along the edges. This is consistent with the often observed tendency for the projected magnetic field direction to wrap around the edges of the hotspot region (see e.g. 3C 445 in Leahy et al. (1997) for a similar overall source structure).

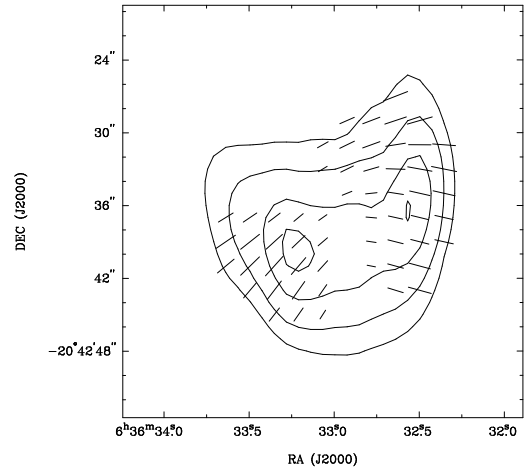


Figure 9. Total intensity (contours) and intrinsic polarization angle (sticks) of southern hotspot of PKS J0636–2036 at 5'' resolution with ATCA at 16 cm band.

4.1.2 ATCA constraints for broadband depolarization modelling

We find no evidence for depolarization within the 16 cm band, by comparing the fractional polarization found using RM synthesis on the upper (> 2.1 GHz) and lower (< 2.1 GHz) frequency ranges of the band. Therefore, the goal here is to extract quantitative information from the ATCA data that can be used as constraints for the broadband polarization model-fitting of the MWA data (Section 4.1.3).

We consider both the integrated polarization and RM properties of the entire hotspot as well as the integrated properties of the two distinct regions of polarization, as identified in Figure 6. By integrating the Stokes Q and U within these two regions (bounded by the dividing line and outer-

most Stokes I contour), we estimate the degree of polarization (p_{ATCA}) of each region with respect to the integrated emission of the entire hotspot (as this is the quantity determined by the model fitting of the MWA data). We find the degree of polarization of the region to the west (Region W) to be $\sim 17\%$, and the region to the east (Region E) to be $\sim 15\%$ (see Table 4).

In order to inform our polarization modelling of the MWA data, we consider polarization-weighted quantities from the ATCA data. We estimate the polarization-weighted mean RM (RM_{wtd}) and polarization-weighted RM dispersion ($d\text{RM}_{\text{wtd}}$), respectively, as

$$\text{RM}_{\text{wtd}} = \frac{\sum_j p_j \text{RM}_j}{\sum_j p_j}, \quad (4)$$

and

$$d\text{RM}_{\text{wtd}} = \left(\frac{\sum_j p_j (\text{RM}_j - \text{RM}_{\text{wtd}})^2}{\sum_j p_j} \right)^{1/2}, \quad (5)$$

where the RM is summed over all pixel locations (j) and weighted by the polarized intensity (p) at each pixel. The polarization-weighted mean and standard deviations of the intrinsic polarization angles ($\psi_{0,\text{wtd}}$ and $d\psi_{0,\text{wtd}}$) were obtained in a similar manner. We only sum over those pixels for which we have obtained RM values (i.e. above a $5\sigma_{QU}$ cutoff).

Table 4 summarises the parameter values calculated in the above manner for the resolved hotspot regions at 16 cm. The variation in RM of $d\text{RM}_{\text{wtd}} = 2.2 \text{ rad m}^{-2}$ is relatively small compared to the mean polarization-weighted RM error of 1.4 rad m^{-2} . However, following Leahy et al. (1986), we find a reduced chi-squared of 3.2 for the significance of the observed RM variations for our $5\sigma_{QU}$ cut-off (3.1 for a $10\sigma_{QU}$ cut-off). A reduced chi-squared of ~ 1 is expected if noise errors dominate the RM fluctuations. By subtracting in quadrature the mean polarization-weighted RM error from $d\text{RM}_{\text{wtd}}$, we get an estimate for the true underlying RM dispersion of 1.7 rad m^{-2} . However, in Section 4.1.3 we find that this is an overestimate of the Faraday dispersion required to explain the observed depolarization for the MWA band.

The intrinsic polarization orientation displays large variations across the hotspot with $\psi_{0,\text{wtd}}$ differing by $\sim 52^\circ$ between Regions E and W. Within Region E, there is a relatively small systematic variation in its intrinsic polarization orientation ($\lesssim 20^\circ$), while Region W displays a larger systematic change in the field orientation of $\sim 40^\circ$ from the south towards the north-eastern edge (Fig. 9).

In our approach to modelling the MWA data (Sections 3 & 4.1.3), we assume that each ‘RM component’ is well characterised by a constant intrinsic polarization angle. This assumption of distinct regions of constant intrinsic field orientation dominating the emission is, in detail, inconsistent with the observed high resolution polarization structure. This is not overly surprising given the complex total intensity and polarization structure observed in hotspots at high angular resolution (e.g. Leahy et al. 1997; Tingay et al. 2008). Additionally, we expect some diffuse polarized emission has been resolved out in our ATCA observations that is present in the MWA data. This highlights some limitations of our polarization modelling approach in the presence

Table 4. Summary of ATCA data for southern hotspot.

	p_{ATCA} (%)	RM_{wtd} (rad m^{-2})	$d\text{RM}_{\text{wtd}}$ (rad m^{-2})	$\psi_{0,\text{wtd}}$ (deg)	$d\psi_{0,\text{wtd}}$ (deg)
Region E	14.7	49.4	1.8	-43.6	5.7
Region W	17.3	50.1	2.3	-96.0	11.5
All	15.2	49.7	2.2	-71.1	27.8

Note: Col. 1: Region of hotspot. Col. 2: Degree of polarization at 16 cm. Col. 3: polarization-weighted RM. Col. 4: polarization-weighted standard deviation in RM. Col. 5: polarization-weighted intrinsic polarization angle. Col. 6: polarization-weighted standard deviation in the intrinsic polarization angle.

of significant underlying polarization and Faraday rotation structure. However, in the context of hotspots which can have significant structure on scales of 10^3 ’s of parsecs (see Tingay et al. 2008, and references therein), this will remain an issue even with high angular resolution spectropolarimetry at low frequencies. The development and application of more detailed polarization models is required but beyond the scope of the current work.

4.1.3 Depolarization modelling

We applied our polarization model-fitting techniques (Section 3) to the RM synthesis-averaged $p(\lambda^2)$ data (Section 4.1) in order to investigate the physical cause of the observed depolarization behaviour. We fit the polarization models to the $p(\lambda^2)$ data instead of the $q(\lambda^2)$ and $u(\lambda^2)$ data because we lack an absolute calibration of the polarization angle across the five MWA bands.

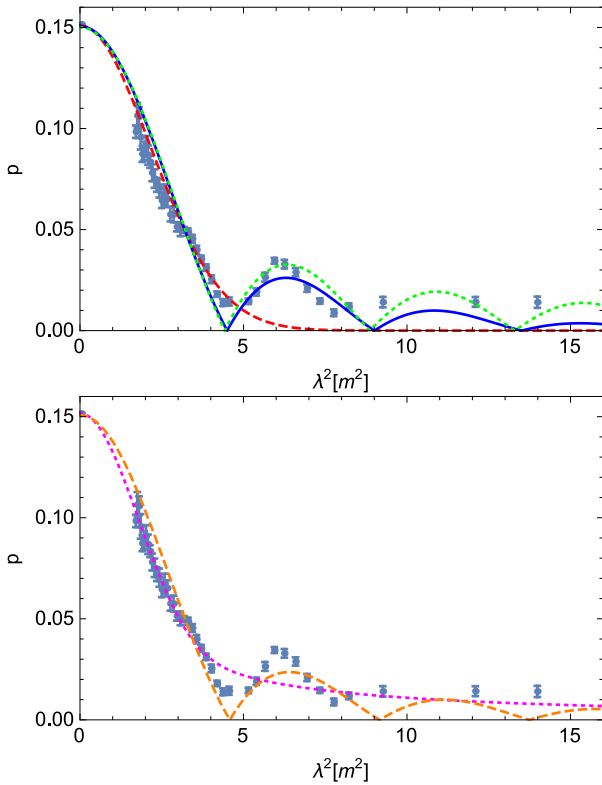
Table 5 lists the best-fitting one-RM-component model parameter values for the southern hotspot data, along with their reduced-chi-squared (χ_r^2) and BIC values. Models (1a), (1b) and (1c) represent Eqn. 2 for different combinations of the Faraday depolarization parameters ($\sigma_{\text{RM,B}}$ and ΔRM , as can be inferred from the table entries themselves). While Models (1d) and (1e) represent Eqn. 3, with and without the ΔRM parameter, respectively. The RM and intrinsic polarization angle are fixed using the values for ‘All’ in Table 4, although variations in the parameters do not change the depolarization curve. As can be seen from the χ_r^2 values and in Figure 10, where we overlay the best-fitting models on the $p(\lambda^2)$ data, none of the one RM component models provide adequate descriptions of the data. Model (1e) is selected by the BIC as the best-fitting model relative to the others. All the models generally describe the initial depolarization reasonably well, requiring a Faraday depolarization of $\Delta\text{RM} \sim 0.7 \text{ rad m}^{-2}$ or of $\sigma_{\text{RM}} \sim 0.2 \text{ rad m}^{-2}$. However, most fail to adequately describe the secondary peak in $p(\lambda^2)$ at $\lambda^2 \sim 6 \text{ m}^2$, as well as the data at longer wavelengths.

The poor performance of the one RM component models, and the results from Section 4.1.2, led us to try models with two RM components. As we are doubling the number of parameters, we expect the fits to improve significantly. However, the BIC (and χ_r^2) strongly penalises additional free parameters, thus providing us with a robust statistical measure as to whether or not the two RM component models are truly better descriptions of the data than the one RM component models (e.g. Schnitzeler 2018).

Table 6 lists the fitted parameter values of the two RM

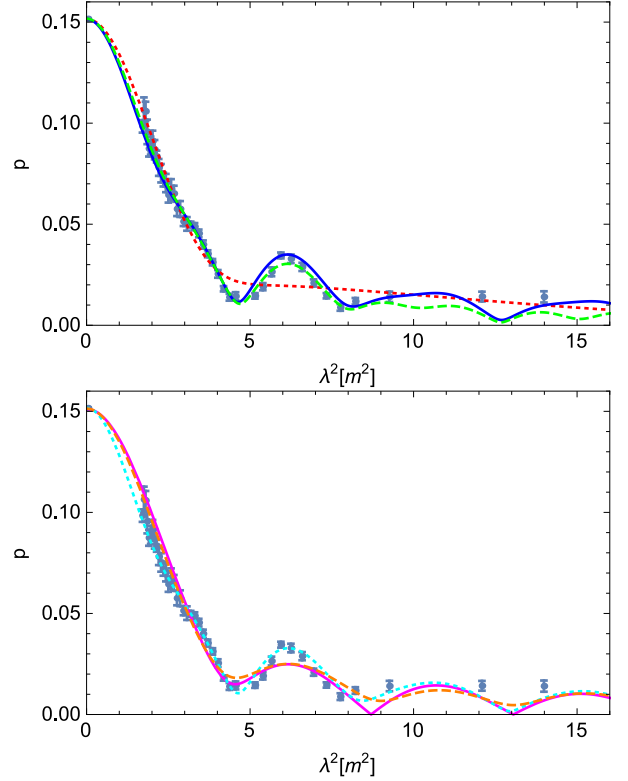
Table 5. Best-fitting parameters for one RM component models.

	p_0 (%)	$\sigma_{\text{RM,B}}$ (rad m ⁻²)	ΔRM (rad m ⁻²)	$\sigma_{\text{RM,T}}$ (rad m ⁻²)	χ_r^2	BIC
(1a)	15.1(2)	0.233(7)	–	–	37	293
(1b)	15.0(1)	–	0.709(8)	–	16	258
(1c)	15.1(1)	0.05(1)	0.698(9)	–	14	255
(1d)	15.0(1)	–	0.69(1)	0.20(5)	14	258
(1e)	15.2(1)	–	–	0.27(1)	11	243

 Note: RM = 50 rad m⁻² for all models.

Figure 10. Plot of the $p(\lambda^2)$ data for the southern hotspot (described in Figure 5 and Section 4.1), overlaid by the best-fitting one RM component models (Table 5). Top: Model (1a), red dashed line. Model (1b), green dotted line. Model (1c), blue solid line. Bottom: Model (1d), orange dashed line. Model (1e), magenta dotted line.

component models, and Figure 11 shows the $p(\lambda^2)$ data overlaid by the best-fitting two RM component models. Models (2a), (2b), (2c) & (2d) represent Eqn. 2 for different combinations of the Faraday depolarization parameters ($\sigma_{\text{RM,B}}$ and ΔRM), in the context of a two RM component model. While Models (2e) and (2f) represent Eqn. 3, for different $\sigma_{\text{RM,T}}$ and ΔRM parameter combinations. Here we have used the information from Table 4 to constrain the RM for both components to 50 rad m⁻² and the intrinsic polarization angles to -96.0° and -43.6° (from Table 4). We also tried fits where RM_1 , $\psi_{0,1}$ and RM_2 , $\psi_{0,2}$ were allowed to vary around their respective values, but we did not find any significant improvements in the fits.

Overall, Model (2c) is the favoured best-fitting model with the lowest BIC and χ_r^2 values, and provides a consid-


Figure 11. Plot of the $p(\lambda^2)$ data for the southern hotspot (described in Figure 5 and Section 4.1), overlaid by the best-fitting two RM component models (Table 6). Top: Model (2a), red dotted line. Model (2b), blue solid line. Model (2c), green dashed line. Bottom: Model (2d), magenta solid line. Model (2e), orange dashed line. Model (2f), cyan dotted line.

erably better fit than the best-fitting one RM component model, Model (1e). However, the value of $\chi_r^2 = 2.1$ indicates that Model (2c) does not fully capture the data and/or the errors in the MWA $p(\lambda^2)$ data are underestimated (by a factor of ~ 1.7). While a more in-depth error analysis of the MWA data may indeed increase the size of the error bars, the simplified assumptions in the depolarization models, as identified in Section 4.1.2, are the most likely limiting factor for the model-fitting. We do not consider three RM component models (or more complex model geometries) mainly because of the large number of model parameters that would need to be fixed due to our inability to do full ‘qu-fitting’ for the current dataset.

Based on the results of Model (2c), we tentatively identify Region E as the component with $\sigma_{\text{RM1,B}} = 0.054 \pm 0.006$ rad m⁻² and $\Delta\text{RM}_1 = 0.725 \pm 0.005$ rad m⁻², and Region W with $\Delta\text{RM}_2 = 1.24 \pm 0.01$ rad m⁻². Reassuringly, the ratio of $p_{0,1}$ and $p_{0,2}$ is 0.85, which is very similar to the ratio of the p_{ATCA} values for Region E & W in Table 4. The lower $p_{0,1,2}$ values are understandable in the context of the large synthesised beam of the MWA. In Section 5, we use the results of Model (2c), in particular the Faraday depolarization parameters, to derive constraints on the properties of the magnetoionic material local to the hotspot.

Table 6. Best-fitting parameters for two RM component models. Overall best-fitting model in bold.

Model	$p_{0,1}$ (%)	$\sigma_{\text{RM1,B}}$ (rad m ⁻²)	ΔRM_1 (rad m ⁻²)	$\sigma_{\text{RM1,T}}$ (rad m ⁻²)	$p_{0,2}$ (%)	$\sigma_{\text{RM2,B}}$ (rad m ⁻²)	ΔRM_2 (rad m ⁻²)	$\sigma_{\text{RM2,T}}$ (rad m ⁻²)	χ_r^2	BIC
(2a)	15.6(1)	0.245(5)	–	–	2.3(4)	0.05(2)	–	–	9.9	240.3
(2b)	12.7(3)	–	0.734(6)	–	12.1(3)	–	1.26(2)	–	3.2	190.8
(2c)	13.4(3)	0.054(6)	0.725(5)	–	11.4(4)	–	1.24(1)	–	2.1	174.7
(2d)	11.2(8)	–	0.72(1)	–	13.4(6)	0.237(5)	–	–	7.7	229.2
(2e)	9.4(1)	–	0.71(2)	–	14.5(5)	–	–	0.252(8)	7.0	227.9
(2f)	12.7(3)	–	0.726(7)	0.11(8)	12.2(4)	–	1.24(2)	–	3.1	195.2

Note: $\psi_{0,1} = -96.0^\circ$, $\psi_{0,2} = -43.6^\circ$, and $\text{RM}_1 = \text{RM}_2 = 50 \text{ rad m}^{-2}$ for all models.

4.2 Northern Hotspot and Bridge

Using the MWA and NVSS data, we find a total intensity spectral index of $\alpha = -0.78 \pm 0.02$ for the northern hotspot region, at $3'.3$ resolution and centred on the peak polarized intensity of the northern hotspot. The average RM for the northern hotspot of $\sim +36 \text{ rad m}^{-2}$ is significantly lower ($\sim 14 \text{ rad m}^{-2}$) than the southern hotspot. While it is possible that this RM difference is due to an asymmetry in the environment on either side of the host galaxy, we consider it more likely that the difference is due to a variation in the Milky Way RM on a scale of $\sim 15'$.⁵

To analyse the depolarization behaviour, we use the MWA band-averaged polarization data (Table 3), as the low signal to noise in polarization does not allow us to reliably extract sub-band information. Thus, we do not sample enough of the depolarization curve to accurately model the depolarization behaviour (Figure 12). However, combining the MWA and NVSS data, and using the Tribble-law for depolarization (Eqn. 3), we can roughly estimate the amount of Faraday depolarization as $\sigma_{\text{RM,T}} \sim 0.9 \text{ rad m}^{-2}$ from an intrinsic degree of polarization of $\sim 11\%$ (Figure 12). We do not have enough data points to reliably constrain a two RM component model. More data is required between 1.4 GHz and 300 MHz, along with more sensitive low frequency data, to constrain the Faraday structure of the northern hotspot in a similar manner as the southern hotspot.

We also detect faint polarized emission from the northern bridge, at J2000 $06^{\text{h}}36^{\text{m}}32^{\text{s}}.8, -20^\circ 32' 15''$. The polarized emission (found at $\sim +38 \text{ rad m}^{-2}$) is fainter than the sidelobes from the southern hotspot at this location. However, the peaks are sufficiently separate in Faraday depth space to estimate a degree of polarization of $\sim 1.2\%$ at 216 MHz and $\sim 0.6\%$ at 185 MHz (it is undetected in the lower frequency bands). We attempted to improve the quality of the FDF at this location by deconvolving the I, Q, U images averaged over 0.64 MHz. However, this did not improve the FDF at this location in a significant manner because for these observations the MWA beam is not well constrained at the location of the source. From the NVSS I, Q, U data smoothed to the MWA resolution, we find this region is $\sim 10\%$ polarized at 1.4 GHz. A Faraday depolarization of $\sigma_{\text{RM,T}} \sim 1.0 \text{ rad m}^{-2}$ can decrease this to the observed degree of polarization in the MWA band.

The ATCA data (Figure 13) show that bright polarized

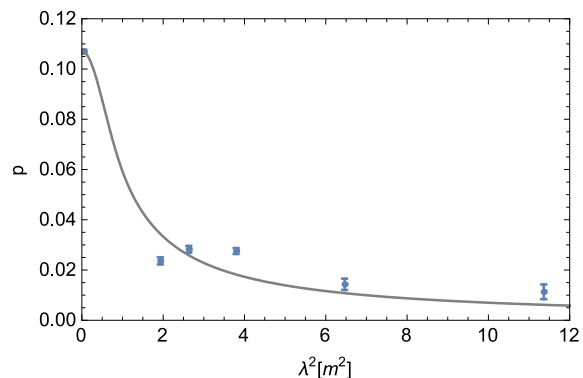


Figure 12. Plot of $p(\lambda^2)$ for the northern hotspot region (blue data points) from MWA and NVSS (see Section 4.2). The solid line shows a single RM component model with a Faraday depolarization of $\sigma_{\text{RM,T}} \sim 0.9 \text{ rad m}^{-2}$ and an intrinsic degree of polarization of $\sim 11\%$.

emission is present south-east of the peak in the total intensity emission. The polarized emission extends further south along the lobe structure until it is too faint to reliably detect. The RM varies across this region from approximately $+34 \text{ rad m}^{-2}$ to $+38 \text{ rad m}^{-2}$ (with a degree of polarization varying from $\sim 16\%$ to $\sim 37\%$ in a north-south direction). Observations with better uv -coverage and sensitivity are required to study the resolved polarization and RM structure of the northern hotspot and lobe in more detail.

5 PHYSICAL INTERPRETATION OF THE OBSERVED FARADAY DEPOLARIZATION

In determining the magnetoionic properties of the gas local to the radio galaxy, we focus solely on the results from the southern hotspot. We consider the two main possible scenarios to explain the Faraday depolarization results, in the context of the expected hotspot environment (Figure 14): internal Faraday rotation (from low-energy relativistic electrons, or from thermal gas internal to the synchrotron emitting region), and external Faraday rotation from magnetised thermal gas outside the radio galaxy.

5.1 Internal Faraday depolarization

Ideally X-ray data would be used to constrain the magnetic field strength in the hotspot without the need for

⁵ The Galactic coordinates of the radio galaxy are $(l, b) = (229.9^\circ, -12.4^\circ)$.

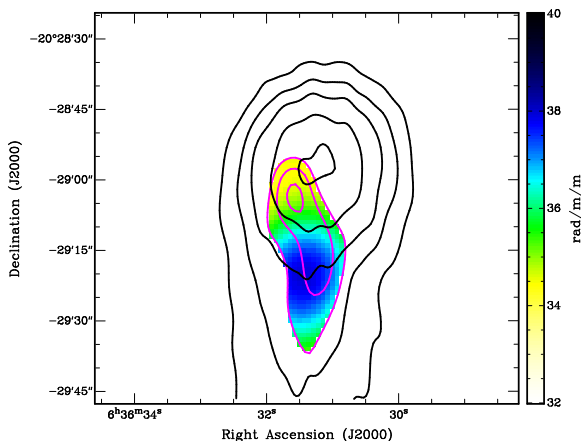


Figure 13. Total intensity (black contours), polarized intensity (magenta contours) and rotation measure distribution (colour-scale) of the northern hotspot at 25'' resolution with the ATCA at 16 cm.

the assumption of equipartition (Harris et al. 1994), but X-ray data for the southern hotspot are currently not available. However, several studies of hotspots in high-luminosity FRIIs find that synchrotron self-compton (SSC) models can explain the radio and X-ray hotspot data, with hotspot magnetic field strengths similar to those derived from the equipartition/minimum energy condition (Hardcastle et al. 1998b, 2002). In low-luminosity FRIIs the comparison is more complicated due to additional X-ray synchrotron emission (Hardcastle et al. 2004, 2016).

We use the synchrotron minimum energy (equipartition) magnetic field formulation described in Worrall & Birkinshaw (2006), which recasts the traditional formulation based on the maximum and minimum radio frequencies (e.g. Longair 2011) to the more physically meaningful low and high relativistic-electron energy distribution cutoffs (γ_{\min} , γ_{\max}). We find an equipartition magnetic field strength of $B_{\text{eq}} \sim 20 \mu\text{G}$, using the observed radio flux for the southern hotspot (Table 3) and the best-fitting spectral index of $\alpha = -0.8$, considering the hotspot as a sphere of radius 10 kpc. Based on SSC model results for hotspots (Hardcastle et al. 2004, 2016), we assume a hotspot volume completely filled with relativistic leptons (filling factor $f = 1$ and $k = 0$)⁶ with $\gamma_{\min} = 1000$.

We cannot constrain the value of γ_{\min} from our observations as we do not detect any evidence of a turnover of the total intensity spectrum of the hotspot at the lowest frequencies (Fig. 3), which could indicate the presence of a low-energy cutoff in the relativistic electron energy distribution (e.g. Carilli et al. 1991). However, many studies suggest that γ_{\min} is somewhere between 100 and 1000 for FRII hotspots (Carilli et al. 1991; Hardcastle et al. 1998a; Godfrey et al. 2009; McKean et al. 2016). Moderate filling factors and a proton population that does not dominate the energetics are still consistent with SSC model predictions (Hardcastle et al. 2004), so in principle a magnetic field strength of up to $B_{\text{eq}} \sim 70 \mu\text{G}$ may still be possible ($f = 0.1$,

⁶ k is the ratio of total energy in non-radiating particles to that in synchrotron-emitting leptons.

$k = 1$, $\gamma_{\min} = 100$). However, based on the most likely parameters from the SSC modelling and for simplicity, we use $B_{\text{eq}} = 20 \mu\text{G}$.

5.1.1 Internal Faraday depolarization from thermal gas

Ordered polarization structures in FRII hotspots (and elsewhere in radio galaxies) are most commonly considered to arise from the stretching and compression of an initially disordered magnetic field by the flow of the relativistic plasma (Laing 1980). Although current three dimensional MHD simulations indicate that large-scale ordered fields likely exist in the jet launching region (e.g. McKinney & Blandford 2009) and possibly persist to kiloparsec scales (Tchekhovskoy & Bromberg 2016), there is of yet no strong observational support for this scenario in relation to radio galaxy hotspots. Therefore, we assume the partially ordered field responsible for the observed degree of polarization is effectively random in the context of the line of sight magnetic field (B_{\parallel}) responsible for the Faraday rotation.

Internal Faraday rotation may occur within the hotspot itself or in the surrounding lobe material. Based on the assumptions used to estimate B_{eq} , it is unlikely that the hotspot contains a significant amount of thermal plasma. However, significant amounts of thermal plasma could in principle exist in the surrounding lobe material. As the supersonic jet terminates at the hotspot region, the shock-accelerated material flows backwards to inflate an over-pressured cocoon/lobe surrounding the jet (Figure 14). If this ‘backflow’ entrains thermal gas from the environment, through surface-wave instabilities for example (Bicknell et al. 1990), then it may be a significant source of Faraday depolarization.

For $\Delta\text{RM} \sim 0.7 \text{ rad m}^{-2}$ due to internal Faraday rotation, then following Eqn. 1, we estimate an average internal thermal electron density of $n_e \sim 10^{-4} (N_{\text{rev}}/1000)^{1/2} \text{ cm}^{-3}$, using a path length of twice the radius of the hotspot, $B_{\parallel} = B_{\text{eq}}/\sqrt{3}$ and assuming B_{\parallel} reverses direction of order 1000 times along the path length (N_{rev}).

5.1.2 Internal Faraday depolarization from low-energy relativistic electrons

In light of the small observed Faraday depolarization, we now consider internal Faraday rotation from purely relativistic particles in the hotspot. In this regard, it is the relativistic electrons at the low energy end of the electron energy spectrum that contribute most to the internal Faraday rotation. As there is no Faraday rotation in a pure pair plasma, we require an excess of low-energy electrons (or positrons). Following Jones & O’Dell (1977) and Homan (2012), we have the RM from relativistic particles (RM_r),

$$\text{RM}_r \sim \frac{1.6 \log \gamma_{\min}}{\gamma_{\min}^2} \int_L^0 n_r B_{\parallel} dl \quad (6)$$

for $\alpha = -0.8$ and where n_r is the relativistic particle number density and all units are the same as before. Using the equipartition condition, we can write the relativistic particle density in terms of γ_{\min} and the magnetic field strength, giving $n_r \sim 1.8 \times 10^{11} B^2 \gamma_{\min}^{-1} \text{ cm}^{-3}$ (e.g. Godfrey et al. 2012).

For $\gamma_{\min} = 1000$ and $B_{\text{eq}} = 20 \mu\text{G}$ we find a negligible value of $\text{RM}_r \sim 10^{-8} \text{ rad m}^{-2}$. Thus, this scenario can be ruled out for self consistent parameters related to the hotspot emission.

5.2 External Faraday depolarization

The most common explanation for Faraday depolarization in radio galaxies is depolarization caused by turbulent, magnetised thermal gas in the intragroup/intracluster medium in which the radio galaxy is expanding into (e.g. Laing et al. 2008). In the case of the southern hotspot, we have a compact emission region at a distance of ~ 500 kpc from its host galaxy, in an isolated environment (Baum et al. 1988).

Without deep X-ray observations to reliably determine the external particle number density, we are left to estimate it by other means. A plausible particle number density for the intergalactic medium at the distance (r) of the hotspot, can be estimated using a standard profile $n_{\text{IGM}}(r) \sim n_0(r/a_0)^{-b}$. This gives $n_{\text{IGM}}(500 \text{ kpc}) \sim 3 \times 10^{-5} \text{ cm}^{-3}$, for the typically derived values of $n_0 \sim 10^{-2} \text{ cm}^{-3}$, $a_0 \sim 10$ kpc, and $b \sim 1.5$ (Mulchaey & Zabludoff 1998; Sun 2012). However, the uncertainty in the applicability of these scaling-relations to such an isolated galaxy system as PKS J0636-2036, and the large scatter in the scaling parameters, means that this external gas number density value is quite crude, and possibly overestimated. In the case that this radio galaxy extends into an extremely low density environment, then it may be propagating in the warm-hot intergalactic medium (WHIM), which has an expected particle density of $n_{\text{WHIM}} \sim 10^{-6} \text{ cm}^{-3}$ (e.g. Subrahmanyan et al. 2008; Machalski et al. 2011).

5.2.1 External Faraday depolarization due to a magnetised IGM

In order to estimate physical quantities from the ΔRM parameter, we need to include the correction factor of 1.35 for the case of a linear RM gradient in a Gaussian beam profile (Section 3). For Model (2c), this gives $\Delta\text{RM}_1^c \sim 0.5 \text{ rad m}^{-2}$ and $\Delta\text{RM}_2^c \sim 0.9 \text{ rad m}^{-2}$ (where the c superscript denotes the ‘corrected’ values). Explaining $\Delta\text{RM} \sim 0.5$ to 0.9 rad m^{-2} requires uniform field structures on scales of at least 10 kpc, to produce a smooth gradient in the RM across the emission region. A cell size of 10 kpc and a path length of 500 kpc requires an IGM magnetic field strength (B_{IGM}) of ~ 0.3 to $0.5 \mu\text{G}$ for $n_e \sim 3 \times 10^{-5} \text{ cm}^{-3}$. If the outer scale of the field extends to 500 kpc then $B_{\text{IGM}} \sim 0.04$ to $0.07 \mu\text{G}$. If $n_{\text{WHIM}} \sim 10^{-6} \text{ cm}^{-3}$ is more appropriate for the IGM at the distance of the hotspot, then the required magnetic field strengths are ~ 30 times larger.

5.2.2 External Faraday depolarization due to shock-enhanced IGM gas

An alternative scenario for external Faraday depolarization is from ambient gas that has been compressed and heated by the bow shock from the advancing hotspot (see Figure 14). While strong bow shocks around FRII radio galaxies are expected due to the supersonic advance of the hotspot (Kaiser & Alexander 1997), there is of yet little evidence for

such strong shocks surrounding powerful radio galaxies (although see Stawarz et al. (2014) for a scenario for why these shocks might be difficult to detect in X-ray observations).

Evidence for this scenario has been presented previously in the case of the FRII radio galaxy, Cygnus A (Carilli et al. 1988). They associated an approximately ‘hemispherical structure of large RM’ with the hotspot in the eastern lobe of Cygnus A, and considered this as being due to the compression of the IGM by the expected bow shock. Furthermore, as studied by Guidetti et al. (2011, 2012), compression alone of ambient gas is insufficient to explain the systematic RM gradients (or ‘RM bands’) seen in their observations of FRI radio galaxies. They find that ‘magnetic draping’ (Dursi & Pfrommer 2008), where the external magnetic field is swept up and aligned by the expanding radio source, is required (in addition to some compression).

In our case, considering a maximum density compression factor of 4, gives an enhanced external gas number density of $n_e \sim 1.2 \times 10^{-4} \text{ cm}^{-3}$. The extent of the bow-shocked region is unclear but rough estimates can be made based on numerical simulations of jets in which an extent of approximately 1 to 2 times the size of the hotspot is found (Norman et al. 1982). Assuming that the region of enhanced density and magnetic field extends ~ 20 kpc outside the edge of the radio galaxy, and if the line-of-sight magnetic field does not reverse direction, then we find a shock-enhanced B_{\parallel} ranging from ~ 0.3 to $0.5 \mu\text{G}$ (for $\Delta\text{RM} \sim 0.5$ to 0.9 rad m^{-2}).

This scenario can be quite attractive if the advancing bow-shock has significantly enhanced the gas density and magnetic field strength in this region, in addition to the magnetic-draping effect that generates the initial uniform magnetic field. However, if the IGM density is similar to that of the WHIM ($\sim 10^{-6} \text{ cm}^{-3}$), then the required uniform line-of-sight magnetic field strength in the bow-shocked region becomes quite large ($\sim 10 \mu\text{G}$).

6 DISCUSSION

6.1 Internal or external Faraday depolarization

For internal Faraday rotation from thermal gas, we estimated a thermal electron density of $n_e \sim 10^{-4} \text{ cm}^{-3}$ in the backflow/lobe region surrounding the hotspot (Section 5.1.1). The expected temperature of thermal gas internal to an FRII hotspot/lobe region is unknown. From observations of X-ray cavities associated with radio galaxies, we expect $T > 10$ keV (Schmidt et al. 2002; Gitti et al. 2007) and $T > 500$ keV from models of FRI radio galaxies (Croston & Hardcastle 2014). However, these observations and models do not directly apply to FRII radio galaxies whose jets are not expected to entrain and heat much, if any, thermal material. In any case, if we assume a gas temperature of $T = 500$ keV, then the internal pressure from thermal material is $p_{\text{th}} \sim 2n_e k_B T \sim 3 \times 10^{-11} \text{ Pa}$. We can compare this value to the synchrotron gas pressure of $p_{\min} \sim 10^{-12} \text{ Pa}$, which is ~ 3 times smaller than p_{th} . This is inconsistent with the expectation of thermal gas not being energetically significant in FRII lobes (Croston et al. 2005; Ineson et al. 2017), as opposed to FRI radio galaxies where the opposite is expected to be true (Croston et al. 2008; Birzan et al. 2008; Croston & Hardcastle 2014). Therefore, we consider the case

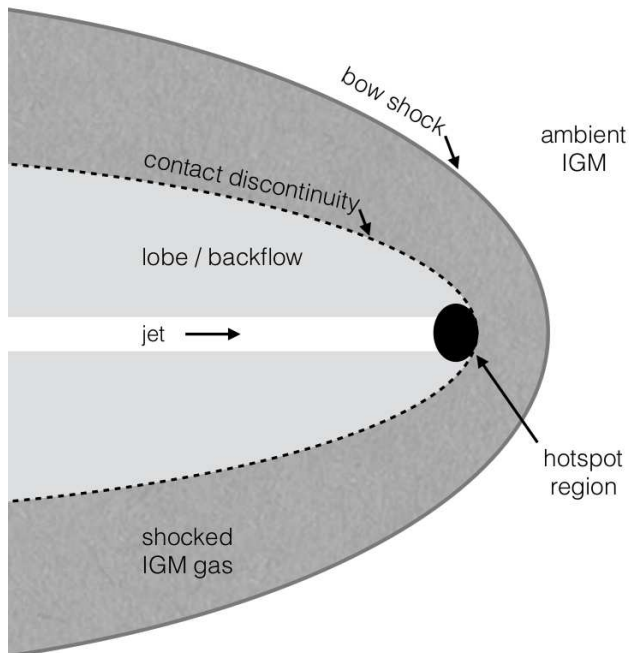


Figure 14. Cartoon illustrating the various components near the termination point of an FR II radio galaxy, as described in Sections 5, to interpret the observed Faraday depolarization.

of significant internal Faraday rotation from thermal gas as unlikely.

For the case of external Faraday depolarization, we lack direct tracers of the ambient thermal gas density. If our extrapolation from group environment scaling relations is close to accurate, then IGM magnetic field strengths ranging from 0.04 to 0.5 μG , for outer and inner field scales of 500 kpc and 10 kpc, respectively, can explain the observed amounts of Faraday depolarization. In both cases, the estimated field strengths would increase by a factor of ~ 30 if the external gas number density is similar to that expected for the WHIM. Such high field strengths would be inconsistent with recent upper limits for intergalactic filaments (Brown et al. 2017; Vernstrom et al. 2017). Therefore, an ambient gas density of order 10^{-5} cm^{-3} is probably more realistic than a WHIM density of $\sim 10^{-6} \text{ cm}^{-3}$. A scenario in which an advancing bow-shock has significantly enhanced the gas density and magnetic field strength over a short range in the ambient medium can also explain the observations, with field strengths in the range 0.3 to 0.5 μG .

From this analysis we can conclude that external Faraday rotation is most likely the dominant factor in the observed depolarization, although the external field strength and scales are not very well constrained. Improved constraints may be obtained from high resolution radio observations at low frequencies, which would better map the RM variations and depolarization across the hotspot region (instead of relying on the depolarization modelling of the integrated hotspot emission). Deep X-ray observations could help to better determine the magnetic field strength in the hotspot, however detecting the ambient thermal gas (shocked or not) would be extremely challenging for current X-ray telescopes.

6.2 A giant radio galaxy

The observed linear size of PKS J0636–2036 on the sky is ~ 957 kpc, putting it just short of the usual size of at least 1 Mpc for classification as a Giant Radio Galaxy (GRG). The axial ratio (R_T , lobe length divided by half the lobe width) of the source ranges from ~ 5 (nearest the host galaxy) to ~ 10 (near the outermost regions). This is more similar to that measured for double radio galaxies (DDRGs) with $9 \lesssim R_T \lesssim 16$ than “normal” FRIIs with $2 \lesssim R_T \lesssim 5$ (Machalski et al. 2011). DDRGs are indicative of recurrent jet activity in which the restarted jet propagates in an underdense environment leading to their large axial ratios. In applying this to GRGs, Machalski et al. (2011) raised the possibility of diffuse emission beyond the hotspot of GRGs with large axial ratios. This would mean that the implied low density of the IGM surrounding GRGs was as a result of a previous epoch of jet activity. However, while not directly invalidating this model, we do not see any evidence for diffuse emission beyond the hotspots, for a noise level of $\sigma \sim 0.15 \text{ Jy beam}^{-1}$. Alternatively, the large axial ratio may be due to unusual jet stability (Scheuer 1974, 1982) enabling the jet to advance faster and further into the surrounding medium. Indeed the intrinsically poor environment (in terms of the expected ambient gas density of the IGM) may substantially assist in achieving both the unusual jet stability and large linear size.

The southern lobe is significantly longer than the northern lobe, with a size ratio of ~ 1.3 between the southern and northern lobe. Such an asymmetry in length can be explained by light travel time effects in dynamical models of FR II sources (e.g. Longair & Riley 1979). The expected size ratio $q = (1 + \beta \cos \theta)/(1 - \beta \cos \theta)$, where $\beta = v_h/c$ is the advance speed (v_h) as a fraction of the speed of light (c), and θ is the angle to the line of sight. Using the measured value of $q = 1.3$, then θ must be less than 82.5° . For typical advance speeds of $0.15c$ to $0.3c$ (Best et al. 1995), then θ ranges from 30° to 65° giving de-projected total linear sizes ranging from 1.87 Mpc to 1.03 Mpc, respectively.

However, it may not be the case that the light travel time is the only effect in contributing to the observed size ratio. From a large study of the emission line properties of powerful radio galaxies, McCarthy et al. (1991) found that the more intense emission line gas was on the shorter arm side of the radio galaxy. This indicates that the radio galaxy environment has a potentially important contribution to any asymmetries in the relative lengths of the lobes. The host galaxy of PKS J0636–2036 has extended emission line gas within $20''$ of the host nucleus with an unclear relation to the jet structure (Baum et al. 1988), although a filament to the north may be evidence of a previous interaction between the northern jet and its environment, potentially limiting the growth of the northern lobe compared to the southern lobe. The northern lobe also has a relatively bright emission feature about $240''$ from the core, indicative of significant dissipation of the jet energy in this region, which might also have limited the advance of the northern lobe into the IGM (as compared to the southern jet which appears to dissipate the majority of its energy at the southern hotspot).

In any case, whether or not the true linear size of the radio galaxy is greater than 1 Mpc, it almost certainly will be in the future, as the bright, compact hotspots indicate that

this radio galaxy is still expanding (supersonically) into the IGM. Giant radio galaxies that are observed in the relict phase with a more relaxed, diffuse structure are more likely to be in pressure equilibrium with the IGM and near the end of their life (e.g. [Subrahmanyan et al. 2008](#)).

6.3 Finding more polarized radio galaxies at low frequencies

The current number density of extragalactic polarized sources with the MWA is quite small, estimated at $\sim 1/100 \text{ deg}^{-2}$ in [Lenc et al. \(2016, 2017\)](#). Here we briefly comment on some of the reasons why PKS J0636–2036 is detected in polarization across the full MWA frequency coverage (70 to 230 MHz), along with the future prospects for detecting more polarized source at low frequencies.

Firstly, the large angular size of the source ($\sim 15'$) means that it is well resolved, given the MWA beamsize of $\sim 3.5'$, even though significant structure remains on smaller scales within the hotspot (as identified by the $5''$ ATCA data). Therefore, the effect of beam depolarization is reduced, with regions of different intrinsic polarization and/or Faraday rotation properties being separated on the sky.

Secondly, and likely more importantly, the intrinsically large linear size of the source ($\sim 957 \text{ kpc}$) means that it extends well outside the host galaxy environment and into the tenuous intergalactic medium. This minimises the impact of external Faraday dispersion as a means of strongly depolarizing the emission, as observed in group and cluster environments (e.g. [Laing et al. 2008](#)). Additionally, [Strom \(1973\)](#) found that sources with large angular and linear size had lower depolarization and found that this was most likely due to Faraday dispersion caused by the hot gas environment surrounding the host galaxy ([Strom & Jaegers 1988](#)). As discussed in [Farnsworth et al. \(2011\)](#), even small Faraday dispersions of $\gtrsim 1 \text{ rad m}^{-2}$ are sufficient to depolarize emission below the typical observational detection limits at low frequencies.

Furthermore, the FRII morphology of PKS J0636–2036 means that the brightest features are at the extremities of the radio source (i.e. in the least dense region of the environment), and they are also compact (i.e. the variation in RM across the emission region will be relatively small). This further helps to minimise the effect of external Faraday dispersion. In support of this, a recent catalog of ~ 90 polarized sources at 150 MHz by van Eck et al. (in preparation), finds that the majority of sources are associated with hotspots of FRIIs.

Thirdly, the large Galactic RM of this source (~ 35 to 50 rad m^{-2}) means that the polarized emission in the Faraday dispersion function is shifted away from the instrumental polarization near $\text{RM} \sim 0 \text{ rad m}^{-2}$, making it easier to reliably identify the real emission from the source; although [Lenc et al. \(2016\)](#) circumvented this problem somewhat by using the time-variable RM of the ionosphere.

This means that the most likely candidates for the detection of extragalactic polarized emission at low frequencies are FRII morphology radio galaxies with large linear sizes that are in low galaxy density environments. Low frequency telescopes with high angular resolution are likely to find many more sources than currently possible with the MWA, given the extra constraint for the MWA of large

angular size sources. The high angular resolution currently provided by LOFAR of $\sim 6''$ ([Shimwell et al. 2017](#)) indicates that a much greater number density of extragalactic polarized sources can be detected, possibly up to one polarized sources every three square degrees ([Mulcahy et al. \(2014\)](#), Neld et al. in prep). In the future, the low-frequency component of the SKA can provide further improvements on the ability to detect polarized sources at low frequencies due to improved survey sensitivity and minimal radio frequency interference. However, we expect the ability to obtain high angular resolution images, similar to LOFAR, will be a key additional requirement.

7 CONCLUSIONS

We have presented a broadband polarization and Faraday rotation study of the nearby radio galaxy PKS J0636–2036 ($z = 0.0551$), using data from the MWA at $3'.3$ resolution from 70 to 230 MHz and the ATCA at $5''$ resolution from 1 to 3 GHz. This FRII radio galaxy has a linear size of $\sim 957 \text{ kpc}$, extending well outside its isolated elliptical host galaxy and into the tenuous intergalactic medium. We find no evidence for flattening or a turnover in the total intensity spectrum of either hotspot, down to $\sim 75 \text{ MHz}$. A total intensity spectral index of $\alpha \sim -0.78$ was found for the northern hotspot, while for the southern hotspot $\alpha \sim -0.82$.

We have detected polarized emission from both the northern and southern hotspot of this radio galaxy, as well as part of the northern bridge. The northern hotspot is $\sim 11\%$ polarized at short wavelengths (with the NVSS at 1.4 GHz), and decreases from $\sim 3\%$ to 1% across the MWA band, with an RM of $\sim +35 \text{ rad m}^{-2}$ and an RM dispersion of $\sim 0.9 \text{ rad m}^{-2}$. The polarized emission from the northern bridge is detected down to 185 MHz, and is consistent with a Faraday dispersion of $\sim 1 \text{ rad m}^{-2}$. The degree of polarization of the southern hotspot varies from $\sim 9\%$ to $\sim 1\%$ across the MWA band, at an RM of $\sim 50 \text{ rad m}^{-2}$, and it is $\sim 15\%$ polarized in the NVSS. The depolarization is broadly consistent with an RM dispersion of $\sim 0.7 \text{ rad m}^{-2}$.

This is the first time the broadband polarization behaviour of a radio galaxy has been determined at such low frequencies. The extensive wavelength-squared coverage provided by these observations (~ 1.7 to 16 m^2) demonstrates the increased precision with which Faraday rotation properties can be determined, compared to traditional cm-wavelength facilities (e.g. VLA, ATCA). However, even though the hotspots are resolved from the lobes by the MWA, substantial structure remains within the southern hotspot. The $5''$ imaging with the ATCA reveals two main sub-regions with high degrees of polarization ($\lesssim 45\%$) and an intrinsic magnetic field structure aligned with the edges of the hotspot region.

A general purpose, polarization model-fitting procedure was applied to the data from the southern hotspot to determine the Faraday depolarization parameters. We find that single RM component models cannot describe the broadband depolarization data from this region. Two RM component models provide substantially better fits to the data, although the best-fitting model still does not fully describe the observed data ($\chi^2_{\text{r}} = 2.1$). This is likely due to simplifying assumptions in the input models. In particular, the as-

sumption that each RM component is well characterised by a constant intrinsic polarization angle. This is inconsistent with the structure revealed by the ATCA. This illustrates the need for high angular resolution at low frequencies as well as the development and application of more detailed polarization models.

We find that a magnetised IGM is more likely to be responsible for the majority of the observed depolarization than Faraday rotation internal to the hotspot emission region. However, due to the poorly constrained external gas density, we cannot uniquely determine the origin of the observed Faraday depolarization. For an estimated ambient density of $3 \times 10^{-5} \text{ cm}^{-3}$, IGM magnetic field strengths ranging from 0.04 to $0.5 \mu\text{G}$ are consistent with the observed depolarization, depending on the exact scale size of the fluctuations and the location of the dominant Faraday rotation region (e.g. in a compressed region outside the hotspot or distributed more uniformly in the IGM).

Overall, this work shows the importance of low frequency polarization and Faraday rotation observations in the study of radio galaxies, the impact on their environments and the magnetised properties of the intergalactic medium. Current and future low frequency surveys with LOFAR, MWA-Phase 2 and SKA1-low, should find a much greater number density of extragalactic polarized sources. This will enable powerful statistical studies of the physical properties of the radio galaxy population and the magnetisation of the intergalactic medium.

ACKNOWLEDGEMENTS

S.P.O acknowledges financial support from UNAM through the PAPIIT project IA103416 and from the Deutsche Forschungsgemeinschaft (DFG) under grant BR2026/23. This research was conducted by the Australian Research Council Centre of Excellence for All-sky Astrophysics (CAASTRO), through project number CE110001020. This scientific work makes use of the Murchison Radio-astronomy Observatory, operated by CSIRO. We acknowledge the Wajarri Yamatji people as the traditional owners of the Observatory site. Support for the operation of the MWA is provided by the Australian Government (NCRIS), under a contract to Curtin University administered by Astronomy Australia Limited. We acknowledge the Pawsey Supercomputing Centre which is supported by the Western Australian and Australian Governments. The Dunlap Institute is funded through an endowment established by the David Dunlap family and the University of Toronto. We are grateful to Lukasz Stawarz for helpful discussions and to the referee, Paddy Leahy, for helpful comments on the original version of this paper.

REFERENCES

Baum S. A., Heckman T. M., Bridle A., van Breugel W. J. M., Miley G. K., 1988, *ApJS*, **68**, 643
 Bernardi G., et al., 2013, *ApJ*, **771**, 105
 Best P. N., Bailer D. M., Longair M. S., Riley J. M., 1995, *MNRAS*, **275**, 1171
 Bicknell G. V., Cameron R. A., Gingold R. A., 1990, *ApJ*, **357**, 373

Birzan L., McNamara B. R., Nulsen P. E. J., Carilli C. L., Wise M. W., 2008, *ApJ*, **686**, 859
 Brentjens M. A., de Bruyn A. G., 2005, *A&A*, **441**, 1217
 Brown S., et al., 2017, *MNRAS*, **468**, 4246
 Brügggen M., Kaiser C. R., 2002, *Nature*, **418**, 301
 Burn B. J., 1966, *MNRAS*, **133**, 67
 Carilli C. L., Perley R. A., Dreher J. H., 1988, *ApJ*, **334**, L73
 Carilli C. L., Perley R. A., Dreher J. W., Leahy J. P., 1991, *ApJ*, **383**, 554
 Condon J. J., Cotton W. D., Greisen E. W., Yin Q. F., Perley R. A., Taylor G. B., Broderick J. J., 1998, *AJ*, **115**, 1693
 Croston J. H., Hardcastle M. J., 2014, *MNRAS*, **438**, 3310
 Croston J. H., Hardcastle M. J., Harris D. E., Belsole E., Birkinshaw M., Worrall D. M., 2005, *ApJ*, **626**, 733
 Croston J. H., Hardcastle M. J., Birkinshaw M., Worrall D. M., Laing R. A., 2008, *MNRAS*, **386**, 1709
 Croton D. J., et al., 2006, *MNRAS*, **365**, 11
 Danziger I. J., Goss W. M., Frater R. H., 1978, *MNRAS*, **184**, 341
 Dursi L. J., Pfrommer C., 2008, *ApJ*, **677**, 993
 Enßlin T., Pfrommer C., Miniati F., Subramanian K., 2011, *A&A*, **527**, A99
 Fabian A. C., 2012, *ARA&A*, **50**, 455
 Fabian A. C., Sanders J. S., Allen S. W., Crawford C. S., Iwasawa K., Johnstone R. M., Schmidt R. W., Taylor G. B., 2003, *MNRAS*, **344**, L43
 Farnsworth D., Rudnick L., Brown S., 2011, *AJ*, **141**, 191
 George S. J., Stil J. M., Keller B. W., 2012, *Publ. Astron. Soc. Australia*, **29**, 214
 Gießübel R., Heald G., Beck R., Arshakian T. G., 2013, *A&A*, **559**, A27
 Gitti M., McNamara B. R., Nulsen P. E. J., Wise M. W., 2007, *ApJ*, **660**, 1118
 Godfrey L. E. H., et al., 2009, *ApJ*, **695**, 707
 Godfrey L. E. H., et al., 2012, *ApJ*, **755**, 174
 Guidetti D., Laing R. A., Bridle A. H., Parma P., Gregorini L., 2011, *MNRAS*, **413**, 2525
 Guidetti D., Laing R. A., Croston J. H., Bridle A. H., Parma P., 2012, *MNRAS*, **423**, 1335
 Hardcastle M. J., Birkinshaw M., Worrall D. M., 1998a, *MNRAS*, **294**, 615
 Hardcastle M. J., Alexander P., Pooley G. G., Riley J. M., 1998b, *MNRAS*, **296**, 445
 Hardcastle M. J., Birkinshaw M., Cameron R. A., Harris D. E., Looney L. W., Worrall D. M., 2002, *ApJ*, **581**, 948
 Hardcastle M. J., Harris D. E., Worrall D. M., Birkinshaw M., 2004, *ApJ*, **612**, 729
 Hardcastle M. J., et al., 2016, *MNRAS*, **455**, 3526
 Harris D. E., Carilli C. L., Perley R. A., 1994, *Nature*, **367**, 713
 Harwood J. J., et al., 2016, *MNRAS*, **458**, 4443
 Harwood J. J., et al., 2017, *MNRAS*, **469**, 639
 Heald G., 2009, in Strassmeier K. G., Kosovichev A. G., Beckman J. E., eds, IAU Symposium Vol. 259, Cosmic Magnetic Fields: From Planets, to Stars and Galaxies. pp 591–602, doi:10.1017/S1743921309031421
 Heckman T. M., Best P. N., 2014, *ARA&A*, **52**, 589
 Homan D. C., 2012, *ApJ*, **747**, L24
 Hurley-Walker N., et al., 2014, *Publ. Astron. Soc. Australia*, **31**, e045
 Hurley-Walker N., et al., 2017, *MNRAS*, **464**, 1146
 Ineson J., Croston J. H., Hardcastle M. J., Mingo B., 2017, *MNRAS*,
 Jelić V., et al., 2015, *A&A*, **583**, A137
 Jones T. W., O’Dell S. L., 1977, *ApJ*, **214**, 522
 Kaiser C. R., Alexander P., 1997, *MNRAS*, **286**, 215
 Kronberg P. P., Wielebinski R., Graham D. A., 1986, *A&A*, **169**, 63
 Kronberg P. P., Dufton Q. W., Li H., Colgate S. A., 2001, *ApJ*, **560**, 178

- Laing R. A., 1980, *MNRAS*, **193**, 439
- Laing R., 1989, in Meisenheimer K., Roeser H.-J., eds, *Lecture Notes in Physics*, Berlin Springer Verlag Vol. 327, Hot Spots in Extragalactic Radio Sources. pp 27–43
- Laing R. A., Bridle A. H., Parma P., Murgia M., 2008, *MNRAS*, **391**, 521
- Leahy J. P., Pooley G. G., Riley J. M., 1986, *MNRAS*, **222**, 753
- Leahy J. P., Black A. R. S., Dennett-Thorpe J., Hardcastle M. J., Komissarov S., Perley R. A., Riley J. M., Scheuer P. A. G., 1997, *MNRAS*, **291**, 20
- Lenc E., et al., 2016, *ApJ*, **830**, 38
- Lenc E., et al., 2017, *Publ. Astron. Soc. Australia*, **34**, e040
- Longair M. S., 2011, *High Energy Astrophysics*. Cambridge University Press
- Longair M. S., Riley J. M., 1979, *MNRAS*, **188**, 625
- Machalski J., Jamrozny M., Stawarz L., Koziel-Wierzbowska D., 2011, *ApJ*, **740**, 58
- Mack K.-H., Klein U., O’Dea C. P., Willis A. G., Saripalli L., 1998, *A&A*, **329**, 431
- McCarthy P. J., van Breugel W., Kapahi V. K., 1991, *ApJ*, **371**, 478
- McKean J. P., et al., 2016, *MNRAS*, **463**, 3143
- McKinney J. C., Blandford R. D., 2009, *MNRAS*, **394**, L126
- McNamara B. R., Nulsen P. E. J., 2012, *New Journal of Physics*, **14**, 055023
- Mitchell D. A., Greenhill L. J., Wayth R. B., Sault R. J., Lonsdale C. J., Cappallo R. J., Morales M. F., Ord S. M., 2008, *IEEE Journal of Selected Topics in Signal Processing*, **2**, 707
- Mulcahy D. D., et al., 2014, *A&A*, **568**, A74
- Mulchaey J. S., Zabludoff A. I., 1998, *ApJ*, **496**, 73
- Norman M. L., Winkler K.-H. A., Smarr L., Smith M. D., 1982, *A&A*, **113**, 285
- O’Sullivan S. P., et al., 2012, *MNRAS*, **421**, 3300
- O’Sullivan S. P., Purcell C. R., Anderson C. S., Farnes J. S., Sun X. H., Gaensler B. M., 2017, *MNRAS*, **469**, 4034
- Offringa A. R., van de Gronde J. J., Roerdink J. B. T. M., 2012, *A&A*, **539**, A95
- Offringa A. R., et al., 2015, *Publ. Astron. Soc. Australia*, **32**, e008
- Ord S. M., et al., 2010, *PASP*, **122**, 1353
- Ord S. M., et al., 2015, *Publ. Astron. Soc. Australia*, **32**, e006
- Orrù E., et al., 2015, *A&A*, **584**, A112
- Planck Collaboration. et al., 2014, *A&A*, **571**, A16
- Raftery A. E., 1995, *Sociological Methodology*, **25**, 111
- Rudnick L., 1988, *ApJ*, **325**, 189
- Rudnick L., Saslaw W. C., Crane P., Tyson J. A., 1981, *ApJ*, **246**, 647
- Ruszkowski M., Yang H.-Y. K., Reynolds C. S., 2017, *ApJ*, **844**, 13
- Sault R. J., Teuben P. J., Wright M. C. H., 1995, in Shaw R. A., Payne H. E., Hayes J. J. E., eds, *Astronomical Society of the Pacific Conference Series Vol. 77, Astronomical Data Analysis Software and Systems IV*. p. 433 ([arXiv:astro-ph/0612759](https://arxiv.org/abs/astro-ph/0612759))
- Scheuer P. A. G., 1974, *MNRAS*, **166**, 513
- Scheuer P. A. G., 1982, in Heeschen D. S., Wade C. M., eds, *IAU Symposium Vol. 97, Extragalactic Radio Sources*. pp 163–165
- Schilizzi R. T., McAdam W. B., 1975, *Mem. RAS*, **79**, 1
- Schmidt R. W., Fabian A. C., Sanders J. S., 2002, *MNRAS*, **337**, 71
- Schnitzeler D. H. F. M., 2018, *MNRAS*, **474**, 300
- Schnitzeler D. H. F. M., Banfield J. K., Lee K. J., 2015, *MNRAS*, **450**, 3579
- Schoenmakers A. P., Mack K.-H., de Bruyn A. G., Röttgering H. J. A., Klein U., van der Laan H., 2000, *A&AS*, **146**, 293
- Shimwell T. W., et al., 2017, *A&A*, **598**, A104
- Sokoloff D. D., Bykov A. A., Shukurov A., Berkhuijsen E. M., Beck R., Poezd A. D., 1998, *MNRAS*, **299**, 189
- Stawarz L., et al., 2014, *ApJ*, **794**, 164
- Strom R. G., 1973, *A&A*, **25**, 303
- Strom R. G., Jaegers W. J., 1988, *A&A*, **194**, 79
- Subrahmanyan R., Saripalli L., Safouris V., Hunstead R. W., 2008, *ApJ*, **677**, 63
- Sun M., 2012, *New Journal of Physics*, **14**, 045004
- Taylor A. R., Stil J. M., Sunstrum C., 2009, *ApJ*, **702**, 1230
- Tchekhovskoy A., Bromberg O., 2016, *MNRAS*, **461**, L46
- Tingay S. J., Lenc E., Brunetti G., Bondi M., 2008, *AJ*, **136**, 2473
- Tingay S. J., et al., 2013, *Publ. Astron. Soc. Australia*, **30**, e007
- Tribble P. C., 1991, *MNRAS*, **250**, 726
- Tribble P. C., 1992, *MNRAS*, **256**, 281
- Vernstrom T., Gaensler B. M., Brown S., Lenc E., Norris R. P., 2017, *MNRAS*, **467**, 4914
- Wayth R. B., et al., 2015, *Publ. Astron. Soc. Australia*, **32**, e025
- Wilson W. E., et al., 2011, *MNRAS*, **416**, 832
- Worrall D. M., Birkinshaw M., 2006, in Alloin D., ed., *Lecture Notes in Physics*, Berlin Springer Verlag Vol. 693, Physics of Active Galactic Nuclei at all Scales. p. 39
- de Bruyn G. A. G., 2012, in *Resolving The Sky - Radio Interferometry: Past, Present and Future*. p. 14
- van Haarlem M. P., et al., 2013, *A&A*, **556**, A2

This paper has been typeset from a $\text{\TeX}/\text{\LaTeX}$ file prepared by the author.